Optimizing the Regularization in Broadband Wavefront Control Algorithm for WFIRST Coronagraph

Erkin Sidick*, Byoung-Joon Seo, Brian Kern, David Marx, Ilya Poberezhskiy, and Bijan Nemati
Jet Propulsion Laboratory, California Institute of Technology, 4800 Oak Grove Drive, Pasadena, CA 91109

ABSTRACT

The WFIRST/AFTA 2.4 m space telescope currently under study includes a stellar coronagraph for the imaging and the spectral characterization of extrasolar planets. The coronagraph employs sequential deformable mirrors to compensate for phase and amplitude errors. Using the optical model of an Occulting Mask Coronagraph (OMC) testbed at the Jet Propulsion Laboratory (JPL), we have investigated and compared through modeling and simulations the performance of several actuator regularization-schemes in broadband wavefront control algorithm used to generate dark holes in an OMC, such as a Hybrid Lyot Coronagraph (HLC). Using the concept of a Tikhonov filter constituting the G-matrix, we have explained what the different regularization schemes do to singular-modes during a wavefront control process called Electric Field Conjugation (EFC). In some cases we confirmed the numerical predictions with the testbed measured results. We present our findings in this paper.

Keywords: Coronagraphy, adaptive optics, deformable mirrors, space telescopes, exoplanets

1. INTRODUCTION

NASA's Science Mission Directorate has begun the study phase of the WFIRST-AFTA mission [1-2], with an anticipated launch date early in the next decade. That study included a high-contrast stellar coronagraph to complement the WFIRST instrument. A series of 9 milestones were developed to demonstrate the technology readiness of the coronagraphic instrument under an aggressive schedule. This instrument is baselined to use two separate but compatible modes, a Hybrid Lyot Coronagraph (HLC) [3-6] and a Shaped-Pupil Coronagraph [7-8]. Another design is based around a Phase-Induced Amplitude Apodization Complex-Mask Coronagraph (PIAACMC) [9-10], and is being matured as a backup. Successful completion of all 9 milestones in September 2016 has brought the instrument to NASA Technology Readiness Level 5 (TRL-5).

Last year we reported the contrast result of Milestone 5, a mean contrast of $8.54\text{x}10^{-9}$ with 10% broadband light centered at 550 nm in a full 360-deg dark-hole with a working angle between $3\lambda/D$ and $9\lambda/D$ with arbitrary polarization on the HLC static testbed. The modulated component of this contrast value is $4.09\text{x}10^{-9}$, and the unmodulated one is $4.46\text{x}10^{-9}$ [11-12]. The performance of the HLC static testbed has been improved significantly since then, resulting in a 10% broadband mean contrast of $1.6\text{x}10^{-9}$ (modulated plus unmodulated components) in static HLC testbed. Among other things, the two main factors enabling such improvement are the following: (1) Further updates to the testbed pseudo-star (replaced COTS pinhole with a clean, JPL-made pinhole). This greatly reduced unmodulated starlight residual. (2) Improved wavefront control algorithm approach (regularization schedule). This reduced modulated starlight residual. During an effort to understand why this new actuator regularization schedule (β-schedule) works better than several other conventional approaches used on both the testbed and simulations, we came across a Tikhonov filter and associated singular-mode spectrum [13]. The Tikhonov filer is part of the G-matrix used to generate incremental actuator commands during an EFC session. The singular-mode spectrum can help us understand the differences among different regularization schemes. In this paper we will introduce the concepts of singular-mode, singular-mode spectrum, easy- and hard-modes, as well as strong- and weak-actuator first. Then we will show that the new β-schedule helps the control algorithm to access more hard-modes, and thus achieve better contrast floor as compared to other conventional regularization approaches. We will also show that among the various actuators of DM1 and DM2, the weak-actuators of DM2 contribute the most in combating the hard-modes.

*Erkin.Sidick@jpl.nasa.gov; Phone 1 818 393-7585; Fax 1 818 393-3290; www.jpl.nasa.gov

2. BACKGROUND

2.1 The OMC Optical System

The key elements of the OMC layout in the *xz*-plane is shown in Figure 1. The starlight is delivered to the OMC input pupil (Pupil-1) by a telescope. On the HLC testbed, we use a broadband light source centered at wavelength λ_c=550nm in combination with five 2%-bandpass filters whose passbands are centered at 528, 539, 550, 561 and 572nm, respectively. In simulations, we assume the input broadband light consists of 5 monochromatic light beams whose wavelengths are equal to those listed above. A pair of 48x48 actuator deformable mirrors, DM1 and DM2, is placed in series in a shared collimated beam and forms the WFC subsystem. DM1 is located near the system pupil, and DM2 in the downstream of this pupil. They provide the control of both phase and amplitude errors in the telescope. The coronagraphic subsystem is made of just two elements, a focal-plane mask (FPM) and a Lyot-Stop. The lenses represent the powered elements in the system.

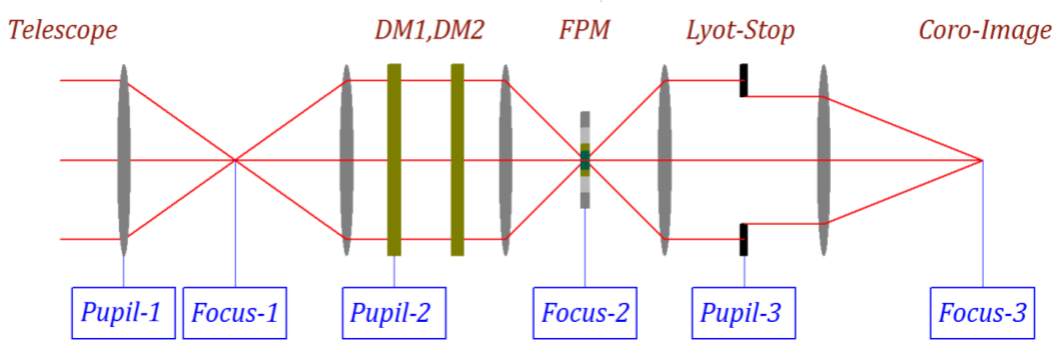

Figure 1. The key elements of the Occulting Mask Coronagraph (OMC) testbed layout. The light source ("starlight") is a collimated beam delivered by a telescope to input pupil (Pupil-1), and a CCD science camera is located at the coronagraphic image (Coro-Image, Focus-3) plane for detecting the image of the "starlight".

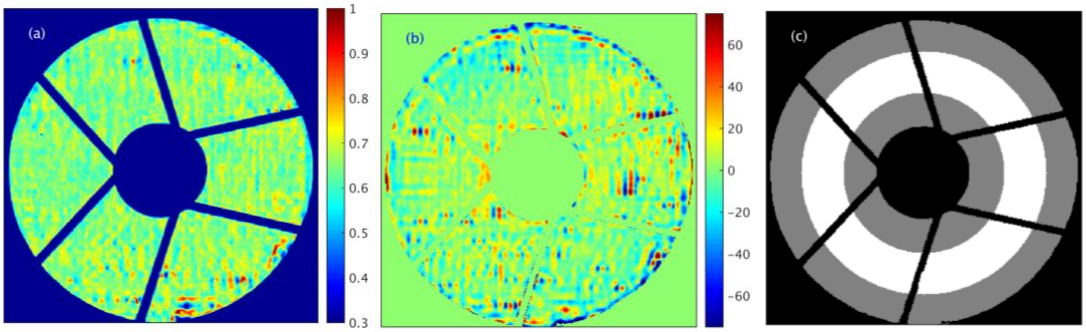

Figure 2. The WFIRST telescope obscuration pattern shown as (a) input pupil amplitude and (b) phase maps. These maps were measured at the Lyot-plane (Pupil-3 in Fig. 1) on the HLC testbed. (c) The Lyot-Stop. The WFIRST pupil, as projected to the coronagraph, is shown in black, the Lyot-Stop in gray, and the pattern of the transmitted light is in white. The phase error map in part (b) is shown as an Optical-Path Difference (OPD) map at the central wavelength of 550nm, and has the root-mean-square (RMS) and the peak-to-valley (PV) values of RMS = 16.7 and PV = 354.7nm, respectively. This map corresponds to a residual phase error obtained after flattening the total system phase errors with two DM's.

The WFIRST telescope pupil is obscured by the secondary mirror and its six support struts. One-pair of the amplitude and the phase maps of the telescope pupil measured at the Lyot-plane of the HLC testbed is shown in Figs. 2(a) and 2(b). The phase in Fig. 2(b) is shown as an Optical-Path Difference (OPD) map at the center wavelength of 550nm, and corresponds to an HLC state after the overall system phase errors are flattened with two DM's. The DMs are used in combination with a focal plane or an occulting mask and a Lyot plane mask, as shown in Fig. 2(c), to generate the high-contrast dark field, as well as to correct for static optical design and manufacturing imperfections and to compensate for

slow thermal drift in the telescope optics. In Fig. 2(c), the WFIRST pupil, as projected to the coronagraph, is shown in black, the Lyot Stop in gray, and the pattern of transmitted light is in white. In all of our subsequent simulations, we include a pair of "Baseline amplitude and WFE maps" in our model, as shown in Figs. 2(a) and 2(b). In our compact PROPER simulation software [14, 15], it is introduced into the input pupil, or Pupil-2 in Fig. 1. These total amplitude and phase error maps exactly correspond to the testbed referenced in this study.

The occulting mask used in both the HLC testbed and our simulations was fabricated by depositing a reflective metal disc on a glass substrate first, then depositing a transparent dielectric layer on top of the metal layer. An atomic force microscope scan of a typical occulting mask is provided on Fig. 10 of Ref. [16].

2.2 Definitions of Normalized Intensity and Contrast

For the current optical system with two DMs, we carry out wavefront control over an annular (360-deg) dark-hole region bound by $R_{\min} = 3\lambda_c/D$ and $R_{\max} = 9\lambda_c/D$, where λ_c= 550nm is the central wavelength, D~=48mm is the diameter of the input pupil aperture, $R = \sqrt{x^2 + y^2}\,/\,f$, and f is the system focal-length. We usually evaluate the contrast performance of the HLC using a normalized intensity and a contrast. The former is defined as

$$I(x,y) = I_o(x,y) / I_{uo\max}\,, \tag{1}$$

where $I_o(x,y)$ is the image intensity of the occulted star, and $I_{uo\max}$ is the peak value of the un-occulted star intensity. It is closely related to the contrast, the metric used most commonly in the fields of high-contrast imaging. The contrast of a field is defined as the planet-to-star flux ratio when the peak pixel of the planet's point spread function (PSF) is equal to the mean per-pixel brightness of the field [15]. We will keep track the value of one metric in this paper, the mean broadband contrast, C_{bb}. The C_{bb} is the mean value of a broadband contrast map inside an annular region from $3\lambda_c/D$ to $9\lambda_c/D$. The broadband image intensity is obtained by simply averaging the narrowband or the monochromatic light intensities at 5 different wavelengths.

2.3 WFC Algorithm and β-Value

In this paper, we use a control algorithm similar to the "minimum-wavefront and optimal control compensator" described in detail in Ref. [17]. This approach is also called "Actuator regularization" and "Electric-Field Conjugation, EFC" [18]. The WFC algorithm described in Ref. [17] uses the wavefront phase at the system exit pupil as its input, and calculates the actuator commands as its output. In the present case of EFC, we set the DM actuators to superpose the negative of the e-field onto the image plane, with a goal to make the image intensity zero on the dark-hole region on the image plane. Therefore, the WFC algorithm uses an e-field column-vector $\vec{\mathbf{e}}$ as its input, where

$$\vec{\mathbf{e}} = \begin{bmatrix} \Re(\vec{\mathbf{E}}) \\ \Im(\vec{\mathbf{E}}) \end{bmatrix}. \tag{2}$$

The joint cost function now becomes as

$$J = \frac{1}{2}\left(\vec{\mathbf{e}}^T\vec{\mathbf{e}} + C_{\mathrm{wu}}\vec{\mathbf{u}}^T\vec{\mathbf{u}}\right), \tag{3}$$

and the gain matrix $\tilde{\mathbf{G}}$ or G-matrix is obtained from

$$\tilde{\mathbf{G}} = \left[\tilde{\mathbf{S}}^T\tilde{\mathbf{S}} + C_{\mathrm{wu}}\tilde{\mathbf{I}}\right]^{-1}\tilde{\mathbf{S}}^T. \tag{4}$$

In Eq. (2), $\vec{\mathbf{E}}$ is the column-vector of the complex e-field on the dark-hole region, and in Eq. (3) the C_{wu} is the actuator regularization coefficient. $\vec{\mathbf{E}}$ is formed by stacking the elements of the complex e-field inside the dark-hole region in a certain order, as was explained in Eq. (1) of Ref. [17]. The $\Re(\vec{\mathbf{E}})$ and the $\Im(\vec{\mathbf{E}})$ are the real and the imaginary parts of $\vec{\mathbf{E}}$, respectively. In Eq. (4), the $\tilde{\mathbf{S}}$ is the sensitivity matrix consisting of the influence functions of all actuators. It is also called "DM actuator response matrix" [15] and "Jacobian" [8].

When operating the HLC testbed, the operator of the testbed does not have direct access to the complex e-field in the coronagraphic image-plane. Therefore, the operator does a wavefront estimation with a pairwise estimation scheme, in

which "probes" are placed on one DM to modulate the electric field across the region of interest [19, 8]. Given two or more pairs of probes, along with an image with no probes at all, both the complex e-field of the residual simulated starlight and the portion of the e-field that does not interact with the probes and hence is unlikely to be correctable can be estimated (The components that do and do not interact with the probes are referred to as the "coherent" and "incoherent" parts, or "modulated" and "unmodulated" components, respectively). More details of the EFC algorithm and its testbed implementation are given in Refs. [18, 8].

Instead of C_{wu}, our testbed team at JPL prefers to use a different regularization coefficient called "β-value". The two coefficients are related by

$$\begin{aligned} \tilde{\mathbf{G}} &= \left[\tilde{\mathbf{S}}^T\tilde{\mathbf{S}} + C_{wu}\tilde{\mathbf{I}}\right]^{-1}\tilde{\mathbf{S}}^T = \left[\tilde{\mathbf{S}}^T\tilde{\mathbf{S}} + \alpha^2\left(10^{\beta}\right)\tilde{\mathbf{I}}\right]^{-1}\tilde{\mathbf{S}}^T \\ \rho &= diag\{\tilde{\mathbf{S}}^T\tilde{\mathbf{S}}\} \\ \alpha^2 &= \max\{\rho\} \end{aligned} \quad , \qquad (5)$$

where "diag" means "diagonal elements", and "max" means "maximum value". One of the advantages of this new choice is that the optimum values of β corresponding to different coronagraph configurations, such as HLC, SPC and PIAACMC, become comparable. That is, the value of α is different for different optical control systems, but the optimum values of β are close to each other. In Eqn. (5), the ρ-value is an indicator of relative actuator strength. In the coronagraph studies we got involved with, the value of C_{wu} is usually positive, but the value of β is usually negative.

The simulation results to be presented in this paper exclude the errors associated with the complex e-field estimation process by obtaining the complex e-field at the final focal plane directly. The simulation creates a 1024x1024-pixel e-field at the final image plane for an aperture of ~305 pixels across, with ~3.6 pixels per $f\lambda_c/D$. Considering only the pixels in the dark-hole and 5 wavelengths gives an e-field vector, $\vec{\mathbf{e}}$, having 32,520 field pixels at $0.3\lambda_c/D$ sampling. There are a total of 48x48x2=4608 DM actuators in the current 2-DM system, but we use only the central 3963 actuators for EFC. So $\tilde{\mathbf{S}}$ has a size of 32,520 x 3,963 pixels.

3. EFFECTS OF β-VALUE ON CONTRAST FLOOR: CONVENTIONAL METHOD

Initially, we obtained a set of DM actuator commands for the "Baseline" conditions of our HLC testbed. These conditions include the measured pupil amplitude and phase maps shown in Figs. 2(a-b), and the translational and the rotational alignment parameters of DM1 and DM2, as shown in Table 1. All of the translational and the rotational parameters of the HLC optics were obtained by characterizing the as-built HLC testbed as best as we can. We also included the actuator command constraints in our simulations [20]. They include: (1) Actuator commands must be within 0 – 100V. (2) The difference of the commands of two neighboring actuators cannot be larger than 30V (neighboring-rule). (3) In DM1, two pairs of actuators are interconnected (paired actuators). Figure 3 shows the normalized intensity maps of this baseline case at 5 different wavelength. The mean broadband contrast value of this case is $C_{bb} = 7.71\text{x}10^{-10}$.

Different researchers follow different approaches when choosing β –values for EFC. The approach used on a testbed also differs from the one used in modeling. Depending on the choice of the β-values, the obtainable best contrast floor can be quite different. For example, Fig. 4(a) shows C_{bb} as a function of control iteration number with β-value as a parameter. Each curve was obtained by using only one β-value shown in the figure legend during an entire EFC session, or during a total of 30 control iterations. Among the cases considered, β = -3 gives the best contrast floor. The initial state of this HLC model was obtained by adding the "Monte-Carlo Error Case #1" of Table 1 to the baseline parameters, using a pupil amplitude measured at a different time relative to the baseline case, and adding some random Zernike-mode and Power Spectral Density (PSD) errors to the baseline pupil phase error map. In Table 1, the "MC Error RMS" column shows the RMS values of the Monte-Carlo errors used to generate the random errors in the next column. The errors introduced as described above degrades the 10%-BW (10% bandwidth) mean contrast from $C_{bb} = 7.71\text{x}10^{-10}$ to $C_{bb} > 10^{-5}$ before carrying out new EFC.

The standard or conventional approach that we have followed in the past when carrying out EFC modeling is to initially start the process with a β -value somewhat greater than a critical value, or β_c, carry out EFC for about 5 iterations, then increase it by 1 and carry out EFC for another number of iterations. After that repeat the latter step for one or more

Table 1. Names of the optical elements and the values of baseline case as well as the misalignment errors used in simulations. "Lyot" means Lyot-Stop, "Occ" the occulting mask, "MC" the Monte-Carlo, "Meas" means "Measured", and "Zern" means "Zernike-mode errors".

Name	Parameter	Symbol	Unit	Testbed Baseline	MC Error RMS	MC Error Case #1
Pupil	Pupil Diameter	D	pix	305.3		
DM1	X-Decenter	Tx	um	-94.1	50	-26.0
	Y-Decenter	Ty	um	-475.1	50	-35.9
	X-Rotation (Tip)	Rx	deg	8.25		
	Y-Rotation (Tilt)	Ry	deg	-0.07		
	Z-Rotation (Clocking)	Rz	deg	-0.86	0.05	-0.06
DM2	X-Decenter	Tx	um	799	50	-42.8
	Y-Decenter	Ty	um	-83.5	50	-45.9
	X-Rotation (Tip)	Rx	deg	2.37		
	Y-Rotation (Tilt)	Ry	deg	0.004		
	Z-Rotation (Clocking)	Rz	deg	0.45	0.05	0
Lyot	X-Decenter	Tx	um		25	34.2
	Y-Decenter	Ty	um		25	3.4
Occ	X-Decenter	Tx	um		0.5	-0.3
	Y-Decenter	Ty	um		0.5	0.4
Pupil Amplitude		Amp		Meas	Meas	Meas
Pupil Phase		Phase		Meas	Zern + PSD	Zern + PSD

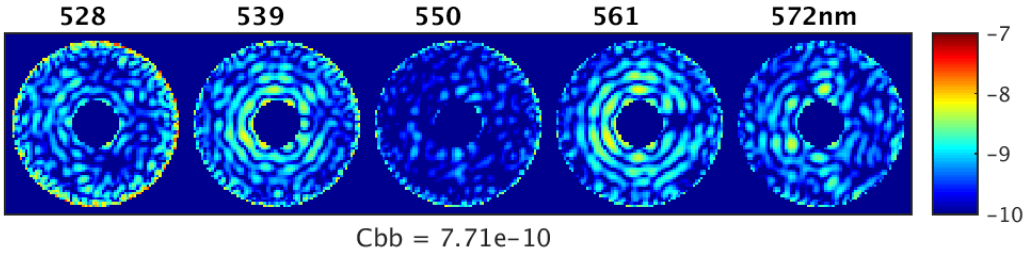

Figure 3. Simulated normalized intensity, $I(x,y)$, of the baseline case inside the $3 - 9\lambda_c/D$ dark-hole region. The 5 intensity maps correspond to five 2% monochromatic beams centered at 528, 539, 550, 561 and 572nm, respectively.

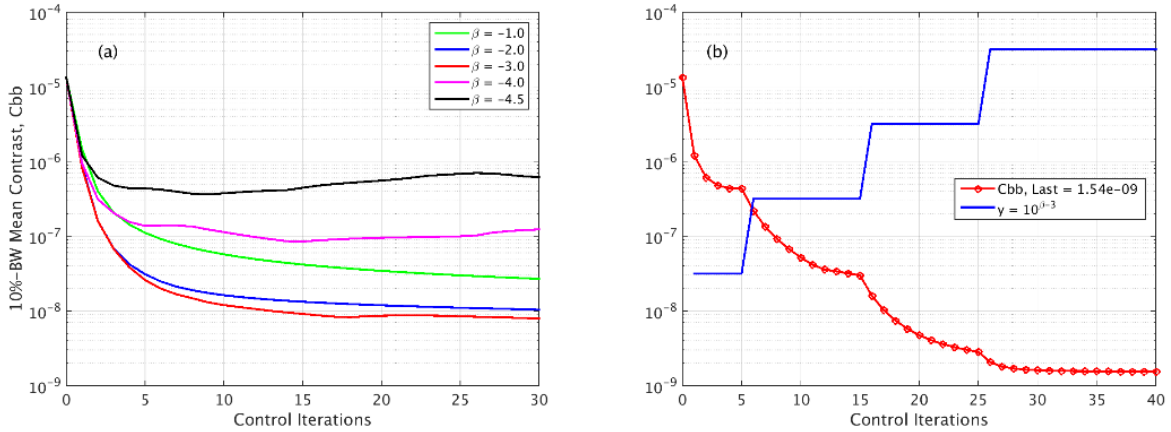

Figure 4. (a) Simulated C_{bb} versus control iteration number obtained with single β-value. The β-values of different cases are listed in the figure legends. (b) Same as part (a), except that the EFC is carried out with 4 different β-values as shown with the blue-lines. In part (b), the blue-curve represents to $y = 10^{\beta-3}$, and is a graphic representation of β-values used.

times. The β_c is defined as the minimum of β such that the EFC process does not diverge during the first few EFC iterations. For example, $\beta_c \sim$ -4.5 in Fig. 4(a). We find β_c by trial and error both on the testbed and in the model. In most cases of simulations, we try values such as β =*a*, *a*+1, *a*+2, where *a* is a constant. In some cases we also carry out a finer search with β = *a*, *a*+0.1, *a*+0.2, and so on.

Following our conventional approach we obtained the C_{bb} versus control iteration number results (red-curve) shown in Fig. 4(b). In this simulation, the EFC process was started with β = -4.5 (blue-curve). Then, after initial 5 iterations, it was increased to β = -3.5. After another 10 iterations it was further increased to β = -2.5. And this step was repeated for one more time with β = -1.5. As we can see, the final contrast floor is much better than all the curves in part (a).

4. NEW β-SCHEDULE AND SINGULAR-MODE HIGH-PASS FILTERS

4.1 New β-Schedule, Tikhonov Filter and Singular-Mode Spectrum

As mentioned above, we reported a 10%-BW mean contrast result of 4.09×10^{-9} (modulated component) last year [12]. By the time of Milestone 9 review was held in January 2017, the HLC static contrast was improved to $C_{bb} = 1.6\times10^{-9}$ (modulated plus unmodulated components). During that period of time both the testbed and its operation strategy were continuously improved. Among other things, there are two important things that had happened during this period of time. One is, testbed team updated the testbed pseudo-star by replacing a COTS pinhole with a clean, JPL made pinhole. This greatly improved the uniformity of the pupil amplitude, and also greatly reduced the unmodulated starlight residual. Figures 5(a,b) and 2(a,b) are the examples of the measured pupil amplitude and phase maps before and after replacing the pinhole. The other is, the testbed team improved the wavefront control algorithm by using a new β-value schedule.

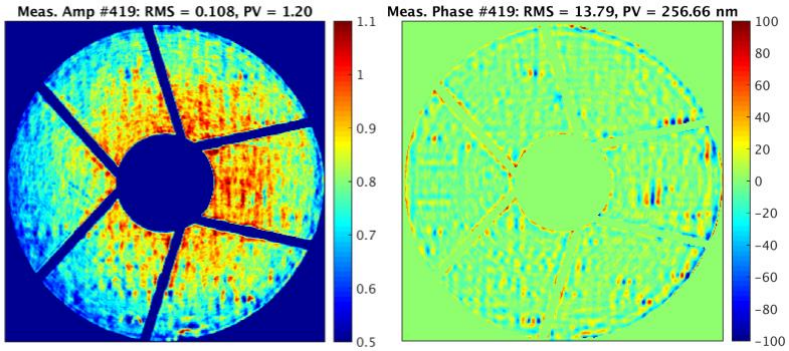

Figure 5. Examples of pupil (a) amplitude and (b) phase measured before replacing the pseudo-star pinhole on the HLC testbed.

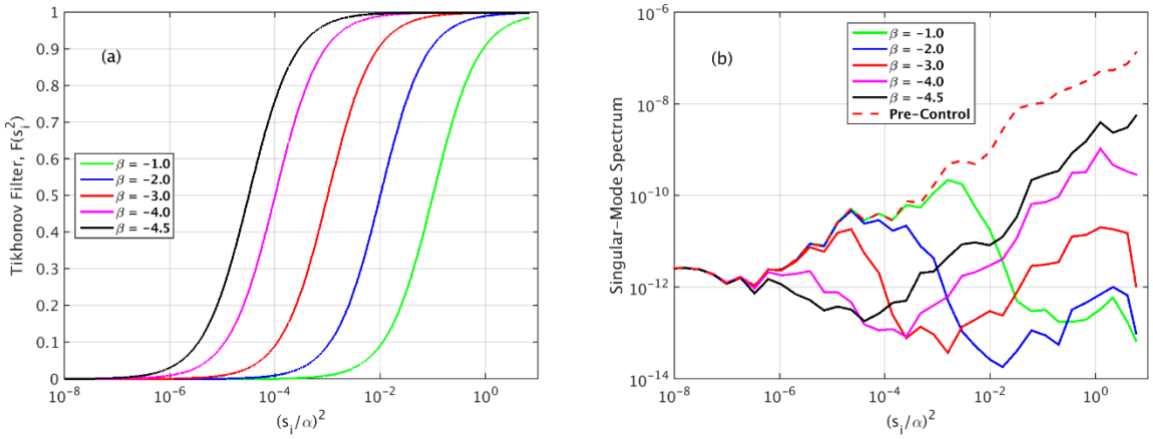

Figure 6. (a) Responses of a Tikhonov filter corresponding to different β-values listed in the figure legends. It is a high-pass filter having a passband of $(s_i/\alpha)^2 \geq 10^{\beta}$. (b) Singular-mode spectra corresponding to the end points (Iter = 30, where "Iter" means Iteration) of C_{bb} in Fig. 4(a).

The other is, the "β-schedule", the sequences by which the β-value is changed during an EFC session, was changed to a new one as explained below.

As illustrated in Ref. [13], the incremental actuator stroke values (or actuator commands), $\Delta\vec{\mathbf{h}}$, can be written as

$$\Delta\vec{\mathbf{h}} = \left[\tilde{\mathbf{S}}^T\tilde{\mathbf{S}} + \alpha^2\left(10^{\beta}\right)\tilde{\mathbf{I}}\right]^{-1}\tilde{\mathbf{S}}^T\vec{\mathbf{e}} = V \times diag\left[\frac{(s_i/\alpha)^2}{(s_i/\alpha)^2 + 10^{\beta}}\frac{1}{s_i}\right]U^{*}\vec{\mathbf{e}} = V \times diag\left[F(s_i)\frac{1}{s_i}\right]U^{*}\vec{\mathbf{e}}$$
$$\tilde{\mathbf{S}} = USV^{*} \quad \text{(Singular – Value Decomposition, SVD)} \quad , \qquad (6)$$
$$s_i = diag(S) \quad \text{(Singuler – Values)}$$

where $F(s_i)$ represents a Tikhonov Filter. Figure 6(a) shows the responses of this filter corresponding to 5 different β-values listed in the figure legends. These β-values are the same at those used in Fig. 4(a). If we define a "Singular-Mode Spectrum", or SMS, as

$$SMS = \left|U^{*}\vec{\mathbf{e}}\right|^2 / \left(N_{\mathrm{DH}} I_{uo\max}\right), \qquad (7)$$

where $I_{uo\max}$ is defined in Eqn. (1) and N_{DH} is equal to the row number of $\tilde{\mathbf{S}}$ divided by 2, and plot the SMS corresponding to the end points (Iter = 30) of C_{bb} curves in Fig. 4(a), then we obtain Fig. 6(b). We can see clearly from this figure that the β-value determines the boundary of singular-modes to be controlled; smaller β-value (or larger |β|-value) means controlling more singular-modes. This is one of the most significant results of this study. It should be pointed out that the sum of *SMS* in Eqn. (7) equals to the 10%-BW mean normalized intensity.

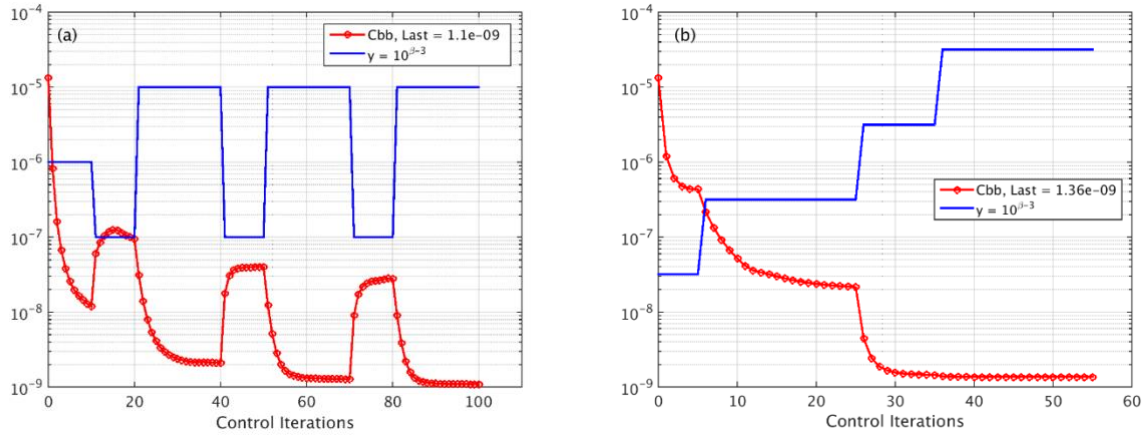

Figure 7. (a) C_{bb} (red-curve) versus control iteration number obtained with new β -schedule (blue-curve). (b) Same as part (a), except that this result was obtained with our conventional β-value approach. The initial condition of these two cases is the same as Fig. 4(a).

The new β –schedule is explained in Fig. 7(a), where the C_{bb} and β–values are plotted as a function of control iteration number. In this approach, we start with a moderate β–value first, then vary it between a pair of low-high values. The numbers of control iterations corresponding to each pair of low-high β steps do not need to be equal, and this ratio can sometimes be adjusted to optimize the final contrast floor. The initial state (Iter = 0) of this simulation is the same as Fig. 4(a). The corresponding result obtained with our conventional β-value approach is shown in Fig. 7(b). In part (a), the Jacobian was updated twice, the first time after Iter = 40 and the second time after Iter = 70. Whereas in part (b) it was updated only once after Iter = 25. In these simulations, the final contrast floor of part (a) is only 24% better than that of part (b), even though the Jacobian was updated twice and a much larger number of control iterations is used. However, such improvement was found to be much better on the HLC testbed than what the simulation here has demonstrated. We believe there are two main reasons for the new β-schedule to work better on the testbed than the simulations here. The first is that the mismatch between the Jacobians of the optical hardware and control algorithm is more severe on the testbed. The second is that the Jacobian is updated almost after every control iteration on the testbed, but we updated it only twice during a 100-iteration EFC session here to shorten the computation time.

The two approaches used to obtain the results of Figs. 7(a,b) produce slightly different singular-mode spectra during their corresponding EFC processes, as shown in Figs. 8(a,b). In Fig. 8(a), starting from Iter = 20, the smaller β-value reduces the modes in the vicinity of $(s_i/\alpha)^2 \sim 10^{-4}$. But during the next higher β-value step the modes in the vicinity of $(s_i/\alpha)^2 \sim 10^{-4}$ achieved during the previous β-step almost remains where there were, but the modes at $(s_i/\alpha)^2 > 10^{-3}$ go down. This process almost repeats itself during the remaining low-high β-steps. But in the case of Fig. 8(b), the modes at $(s_i/\alpha)^2 < 10^{-4}$ almost do not move starting from Iter = 25. This explains why the new β-scheme works better than the conventional β-value method, and is another one of the most significant findings of this study.

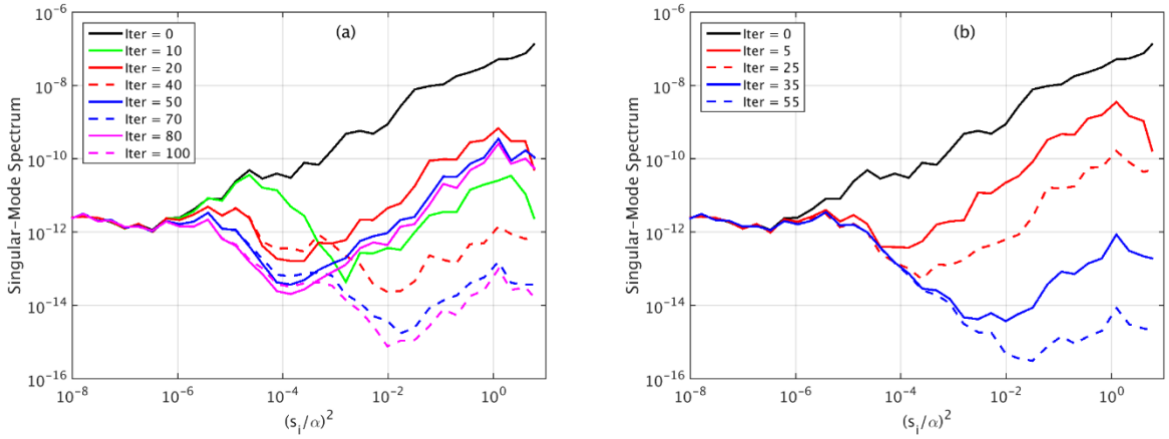

Figure 8. Singular-mode spectra obtained with (a) new β-schedule and (b) the conventional β-value method corresponding to two cases in Figs. 7(a,b).

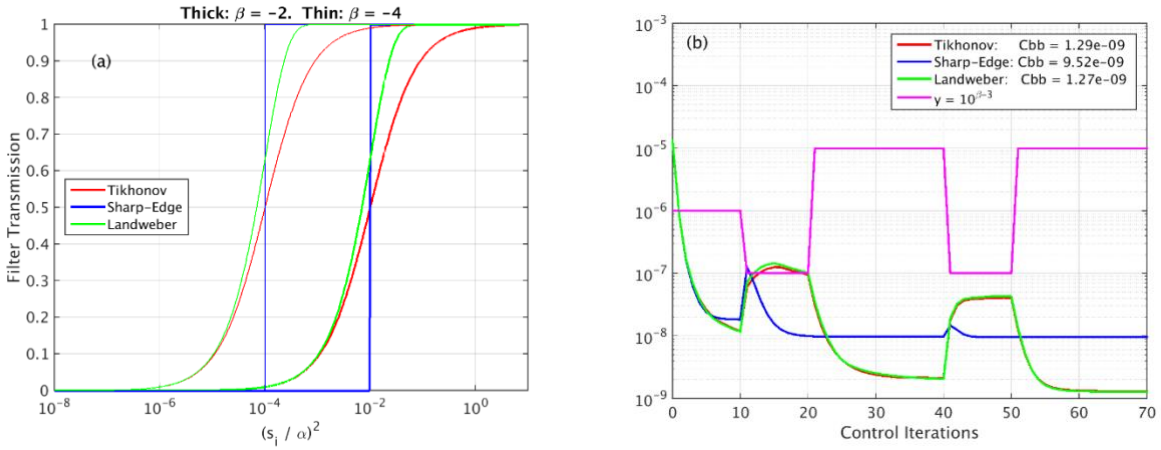

Figure 9. (a) Examples of Tikhonov, Sharp-Edged and Landweber Filter Responses, and (b) C_{bb} versus control iteration number curves obtained with the above 3 types of filters. The pink-curve in part (b) is the plot of $y = 10^{\beta-3}$ and is a graphic representation of the β-values used during these EFC sessions.

4.2 Sharp-Edged (Rectangular, Truncated SVD) and Landweber Filters

After understanding that part of the G-matrix is a high-pass filter, we tried to carry out an EFC session with a rectangular or Sharp-Edged filter, $F_{\text{rec}}(s_i)$, as well as another one with Landweber filter, $F_{\text{lan}}(s_i)$ [13]. They are defined as

$$F_{\text{rec}}(s_i) = \begin{cases} 1, & (s_i/\alpha)^2 \geq 10^{\beta} \\ 0, & (s_i/\alpha)^2 < 10^{\beta} \end{cases}; \qquad F_{\text{lan}}(s_i) = 1 - \left[1 - 0.1 \times (s_i/\alpha)^2\right]^k, \; k = 10^{(1-\beta)}. \tag{8}$$

Figure 9(a) shows examples of the responses of these 3 types of filters, Tikhonov, Sharp-Edged (or Rectangular) and Landweber filters, corresponding to two different β-values. Figure 9(b) compares the corresponding C_{bb} versus control iteration curves. The shape of the Landweber filter response is fairly close to that of the Tikhonov filter, and as a result produces a C_{bb}-curve similar to that of the Tikhonov filter. But the Sharp-Edged filter does not work as well as the other two filters. The pink-lines in Fig. 9(b) is a graphic representation of the β-values used in the corresponding EFC sessions.

5. EASY-HARD MODES AND STRONG-WEAK ACTUATORS

As we can see from Figs. 8(a,b), the singular-modes at $(s_i/\alpha)^2 < \sim 10^{-4}$ are much harder or even impossible to control as compared to the singular-modes at $(s_i/\alpha)^2 > \sim 10^{-4}$. So we can call the singular-modes corresponding to $(s_i/\alpha)^2 < \sim 10^{-4}$ as "hard-modes" and those corresponding to $(s_i/\alpha)^2 > \sim 10^{-4}$ as "easy-modes". One question that naturally comes to mind at this point is if the hard-easy modes are related to the strong-weak actuators or not. In this section we try to find an answer for this question.

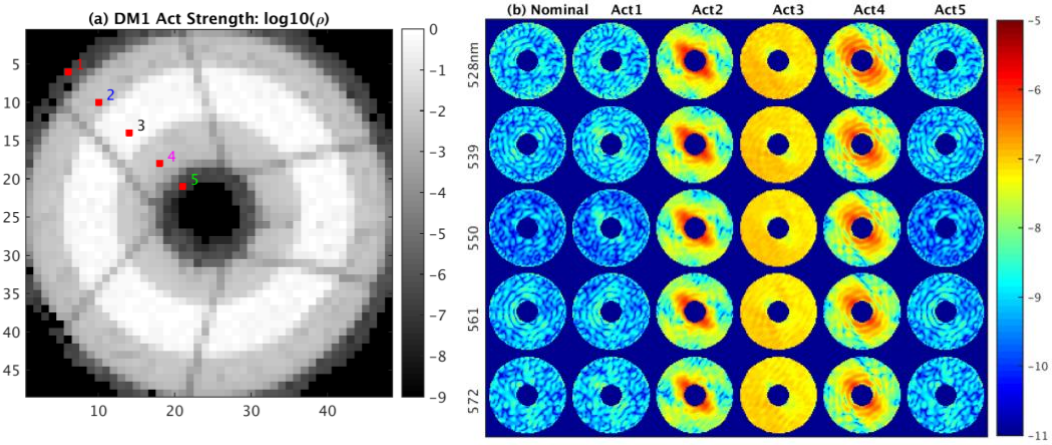

Figure 10. (a) DM1 actuator strength map (ρ-map) and the five actuators chosen for this study. (b) The left-most normalized intensity maps correspond to the last data point in Fig. 7(a), and is referred to as "Nominal Case" here. If we poke the five actuators chosen in part (a), one actuator at a time, and by the stroke values of Δh = 500, 40, 5, 55, 500nm, the normalized intensity maps of the Nominal Case change to the other 5 sets of maps on the right. Note that Act1 is poked by 500nm, Act2 by 40nm, and so on.

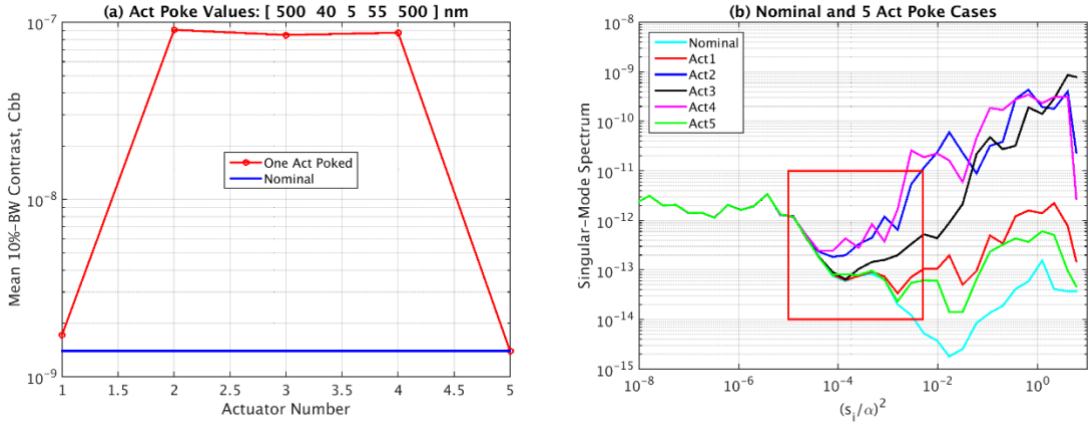

Figure 11. (a) C_{bb}-values corresponding to five single-actuator poking cases in Fig. 10(b). The C_{bb}–value of the nominal case is also shown with a blue-line as a reference. (b) The singular-mode spectra of the six cases shown in Fig. 10(b).

Figure 10(a) shows the actuator strength map of the DM1, or the actuator ρ-values defined in Eqn. (5). We see three distinctive types or groups of actuators from this map: Group-1: Strong actuators projected to the area inside the Lyot-Stop opening. We call this group the "strong actuators". Group-2: Those projected to the area inside the HLC clear

aperture but outside the Lyot-Stop opening. We call this group the "weak actuators". And Group-3: The actuators do not belong to the previous 2 groups. In order to investigate the correlation between these three types of actuators and the corresponding singular-mode spectra, we chose five actuators numbered from 1 to 5 in Fig. 10(a) first. Then, starting from the state corresponding to the last data point in Fig. 7(a), we poked Act1 by 500nm, Act2 by 40nm, Act3 by 5nm, Act4 by 55nm, and Act5 again by 500nm, and obtained the normalized intensity maps shown in Fig. 10(b). The left-most set of maps in this figure corresponds to a "Nominal Case", to the last data point in Fig. 7(a). We chose the poke values of the middle three actuators such that the mean contrast is degraded to about the same level, as shown in Fig. 11(a), where the C_{bb}-values of the five "poked cases" are plotted as a function of actuator order, and the C_{bb} of the nominal case is also shown with a blue-line as a reference. The C_{bb} values of Act1 and Act5 did not change much even when they were poked by an out-of-range value of 500nm because those two actuators are located outside the HLC pupil aperture and have negligible influence to the e-field in the dark-hole image-plane. We can see from the singular-mode spectra of the nominal case and the other five poked cases in Fig. 11(b) that the actuators in Group 2, that is, Act2 and Act4 outside the Lyot-Stop opening but inside the HLC pupil, "excite" the hard-modes in the vicinity of $(s_i/\alpha)^2$ ~10^{-3} (see inside the red-rectangle) much more that the other 3 cases. That is, the weak actuators (Group 2) excite hard-modes more than the strong actuator (Group 1).

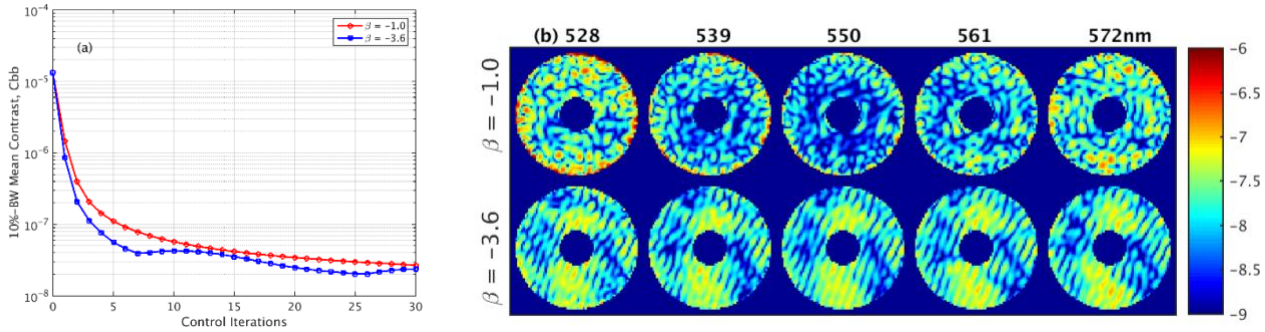

Figure 12. (a) C_{bb} versus control iteration number obtained with single β -value, β = -1 and β = -3.6. (b) Normalized intensity maps corresponding to the last data points in part (a).

To further confirm the relationship between the weak actuators and the hard-modes, we carried out single-β EFC with two β -values for 30 iterations, β = -1 and β = -3.6, such that the resulted final C_{bb} values are close to each other. Obtained mean contrast and normalized intensity map results are shown in Figs. 12(a,b). Although the final C_{bb} values of these two cases are close to each other, the qualitative morphologies of the corresponding $I(x,y)$ maps are somewhat different.

Another big difference between the above 2 cases is in the DM2 actuator commands used. Figures 13(a-d) show the DM actuator commands used to reduce the dark-hole speckles at Iter = 0 of Fig. 12(a) to the one at Iter = 30 in the form of DM-WFE at the pupil. That is, in these plots we converted the actuator stroke map $\Delta h(x,y)$ having a size of 48x48pix into a fine-sampled wavefront error (WFE) corresponding to λ_c = 550nm at the pupil, Pupil-3 in Fig. 1, having a size of ~310x310pix using the HLC model. In order to compare the total strokes of the strong and the weak actuators in a DM, we define a function of merit, FOM, as

$$FOM = \frac{\sum_i |\Delta h(i)|,\ Group2 + Group3}{\sum_i |\Delta h(i)|,\ Group1}. \tag{9}$$

The FOM-value of each case is given as part of the x-label in Figs. 13(a-d). We can see from these figures that the $\Delta h(x,y)$ map and FOM-value of DM1 do not change much between the β = -1 and the β = -3.6 cases, but those of DM2 change a lot. In another word, the weak actuators of DM2 work much harder when β = -3.6 than when β = -1. This result is consistent with what we observed in our investigation explained along with Figs. 10(a,b) and 11(a,b). We can conclude from the above results that in the 2-DM system of HLC, the weak (Group-2) actuators of DM2 contribute much more than the rest of actuators in DM1 and DM2 in combating the hard-modes of this optical system.

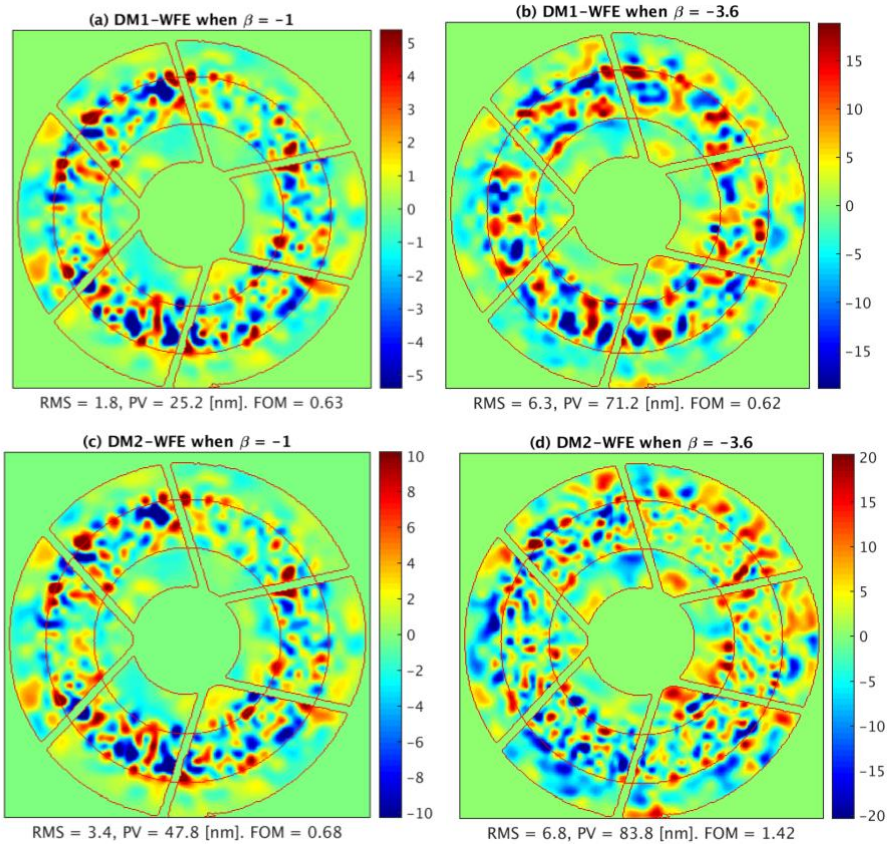

Figure 13. The maps of actuator strokes needed to realize the contrast improvements shown in Fig. 12(a). In these plots the DM actuator strokes are converted into the pupil WFE maps at 550nm, and the term such as "DM1-WFE" is used to indicate such a fact.

6. CONCLUSION

The Hybrid Lyot Coronagraph (HLC) testbed at JPL has completed Milestone 9 with a mean, 10%-broadband total (modulated plus un-modulated) contrast value of 1.6×10^{-9} at a center wavelength of 550nm in a 360-deg dark-hole region covering $3 - 9\lambda_c/D$ field angle. The improvements made on the HLC testbed and its operation since the completion of Milestone 5 last year include the use of a new actuator regularization schedule or β-schedule. In order to understand why this new β-schedule works better than other conventional regularization approaches, we utilized the concept of Tikhonov filter constituting the G-matrix, and introduced several new concepts that have not been used by our research team here at JPL before. The latter include singular-mode spectrum, easy- and hard-modes, and strong- and weak-actuators. The Tikhonov filter explains well what happens to the G-matrix and the singular-modes when we change the β-value during an EFC session.

Tikhonov filter relates the β-value to a passband of singular-modes to be controlled in an EFC process. We have shown that the new β-schedule makes more hard-modes accessible during control, and thus gives better contrast floor as compared to our conventional regularization method. We have also shown that among the strong and the weak actuators of DM1 and DM2, the weak actuators of DM2 work the hardest in combatting the hard-modes. These are part of the significant results of this study. We have also tried other types of high-pass filters, such as Sharp-Edged and Landweber filters. When we replaced the Tikhonov filter with these new ones, Landweber filter performed almost the same as Tikhonov filter, but the Sharp-Edged filter performed much worse than that.

The results of this study greatly expanded our understanding on actuator regularization and EFC, and will help us in the future to find optimum control strategy much more efficiently than before.

The research was carried out at the Jet Propulsion Laboratory, California Institute of Technology, under a contract with the National Aeronautics and Space Administration.

REFERENCES

[1] D. Spergel *et al*, Wide-field Infrared Survey Telescope-Astrophysics Focused Telescope Assets WFIRST-AFTA Final Report, http://wfirst.gsfc.nasa.gov/science/sdt_public/WFIRST-AFTA_SDT_Final_Report_Rev1_130523.pdf (2013).

[2] Ilya Poberezhskiy *et al*, "Technology development towards WFIRST-AFTA coronagraph," Proc. SPIE 9143, 91430P (2014).

[3] *John Trauger, Dwight Moody, Brian Gordon*, "Complex apodized Lyot coronagraph for exoplanet imaging with partially obscured telescope apertures," Proc. SPIE 8864, 886412 (2013).

[4] John Krist, "End-to-end numerical modeling of AFTA coronagraphs," Proc. SPIE 9143, 91430V (2014).

[5] Byoung-Joon Seo, *et al*, "Hybrid Lyot coronagraph for wide-field infrared survey telescope-astrophysics focused telescope assets: Occulter fabrication and high contrast narrowband testbed demonstration," metrics," J. Astron. Telesc. Instrum. Syst. 2(1), 011019 (2015).

[6] John Trauger, Dwight Moody, John Krist, and Brian Gordon, "Hybrid Lyot coronagraph for WFIRST-AFTA: coronagraph design and performance metrics," J. Astron. Telesc. Instrum. Syst. 2(1):011013 (2016).

[7] A. Carlotti, N.J. Kasdin, and R. Vanderbei, "Shaped pupil coronagraphy with WFIRST-AFTA," Proc. SPIE 8864, 886410 (2013).

[8] Eric Cady, *et al*, "Demonstration of high contrast with an obscured aperture with the WFIRST-AFTA shaped pupil coronagraph," J. Astron. Telesc. Instrum. Syst. 2(1):011004 (2015).

[9] Olivier Guyon, "Imaging Earth-like planets around late-type stars with low-inner working angle PIAA coronagraphy," Proc. SPIE 8864, 886414 (2013).

[10] Brian Kern, *et al*, "Phase-induced amplitude apodization complex mask coronagraph mask fabrication, characterization, and modeling for WFIRST-AFTA," J. Astron. Telesc. Instrum. Syst. 2(1):011014 (2016).

[11] Eric Cady, *et al*, "Milestone 5 Final Report: Hybrid Lyot and Shaped Pupil Broadband Contrast Testbed Demonstration for WFIRST-AFTA," http://wfirst.gsfc.nasa.gov/science/sdt_public/wps/references/WFIRST_CGI_Milestone5_Final_Report.pdf.

[12] Erkin Sidick, Byoung-Joon Seo, David Marx, Ilya Poberezhskiy, and Bijan Nemati, "WFIRST/AFTA Coronagraph Contrast Performance Sensitivity Studies: Simulation versus Experiment," Proc. SPIE, vol. 9912, pp. 99126M, August 2016.

[13] Curt Vogel, "Regularization Methods", http://otg.downstate.edu/downloads/2008/Spring08/RefsBMI/Regularization/Inverse-Vogel.pdf.

[14] Erkin Sidick, and F. Shi, "Effect of DM actuator gain errors on the WFIRST/AFTA coronagraph contrast performance," Proc. SPIE, vol. 9605, pp. 9505-5, August 2015.

[15] John Krist, Bijan Nemati, and Bertrand Mennesson, "Numerical modeling of the proposed WFIRST-AFTA coronagraphs and their predicted performances," J. Astron. Telesc. Instrum. Syst. 2(1):011003 (2016).

[16] F. Shi, *et al*, "Low order wavefront sensing and control for WFIRST Coronagraph," Proc. SPIE, vol. 9904, pp. 990418, August 2016.

[17] Erkin Sidick, Scott A. Basinger, and David C. Redding, "An improved wavefront control algorithm for large space telescopes," Proc. SPIE, **7015**, 70154P (2008).

[18] Amir Give'on *et al*, "Broadband wavefront correction algorithm for high-contrast imaging system," Proc. SPIE, **6691**, 66910A (2007).

[19] A. Give'on, B. D. Kern, and S. Shaklan, "Pair-wise, deformable mirror, image plane-based diversity electric field estimation for high contrast coronagraphy," Proc. SPIE 8151, 815110 (2011).

[20] Erkin Sidick, Byoung-Joon Seo, David Marx, Ilya Poberezhskiy, and Bijan Nemati, "Sensitivity of WFIRST coronagraph broadband contrast performance to DM actuator errors," Proc. SPIE, SPIE Conference 10400-6, August 2017.